

EFFECT OF FOOTING ROUGHNESS ON ULTIMATE BEARING CAPACITY OF RIGID STRIP FOOTING ON SANDY SOIL SLOPE

Pham Ngoc Quang*, Pham Ngoc Vinh

The University of Danang - University of Science and Technology, Danang, Vietnam

*Corresponding author: pnquang@dut.udn.vn

(Received: September 9, 2023; Revised: October 16, 2023; Accepted: October 18, 2023)

Abstract - This study investigates the ultimate bearing capacity of a rigid strip footing on a sandy slope using the Rigid Plastic Finite Element Method (RPFEM). To accurately represent a wide range of frictional conditions at the footing roughness, a new interface element was introduced, capable of accommodating both perfectly rough and perfectly smooth conditions. A new constitutive equation is introduced to model these interface elements, which had a significant influence on the failure mode of the strip footing. Moreover, the study focuses on assessing critical parameters, including the internal friction angle of the sandy ground, as well as slope geometry parameters (slope angle β , edge distance L , and slope height H). The RPFEM results illustrate that increasing the edge distance positively influences the bearing capacity, while a higher slope angle exerts a negative effect. Notably, variations in slope height produce consistent outcomes, regardless of the frictional conditions.

Key words - Bearing capacity; Rigid footing; Sandy slope; Rough footing; Smooth footing; RPFEM

1. Introduction

Determining the ultimate bearing capacity of rigid strip footings on sloping terrains is a crucial focus area in geotechnical engineering. The main objective is to establish the maximum load that a strip footing can endure without experiencing failure or excessive deformation. Although established solutions for computing ultimate bearing capacity in horizontal sandy soils are available [1 - 4]. However, the maximum bearing capacity and failure mechanisms of rigid strip footings on sandy slopes continue to be a subject of ongoing research.

Numerous researchers, including [5 - 10] have put forth theoretical and numerical methods for estimating the maximum bearing capacity of footings on sandy slopes. It's worth emphasizing that the ultimate bearing capacity of a rigid strip footing is significantly affected by the frictional conditions at the footing base and the ground surface. Typically, the footing surface is characterized under two extreme conditions: perfectly rough or perfectly smooth. Many previous studies, like those conducted by [10 - 12], have predominantly concentrated on the rough footing, overlooking the influence of smooth footings. This omission raises queries about the impact of footing roughness on the ultimate bearing capacity of the footing-slope system, leaving a comprehensive understanding of the failure mechanism lacking.

To address these challenges, prior investigations conducted by [10, 13 - 16] introduced the concept of employing an interface element to assess the maximum bearing capacity and failure modes of rigid strip footings on level ground. Their findings demonstrated the

effectiveness of utilizing an interface element in these determinations. In the current study, the interface element is extensively utilized to explore failure mechanisms under both rough and smooth footings. The study employs a two-dimensional analysis utilizing the Rigid Plastic Finite Element Method (RPFEM), previously utilized in geotechnical engineering by [17, 18]. Two new constitutive equations are introduced in this study: one for the material of the strip footing and the sandy slope, and another one for interface elements that model the interface plane between the footing base and the ground surface.

This study extensively investigated the effect of various factors, such as soil strength (internal friction angle ϕ), and the geometric parameters of the slope (slope angle, β , slope height, H , and edge distance, L), on ultimate bearing capacity for rough and smooth footings. It also compared these findings with the maximum bearing capacity of horizontal sandy soil, denoted as V_{ult} . The results obtained through RPFEM have provided valuable insights into how these parameters influence the bearing capacity.

2. Methodology for assessing ultimate bearing capacity

2.1. Application of rigid plastic constitutive equation to footing and soil elements

Tamura et al. has derived an elastic-plastic constitutive equation using a Drucker-Prager type yield function as Eq. (1). The yield function is expressed using the first invariant of the stress tensor ($I_1 = \text{tr}(\boldsymbol{\sigma})$) and the second invariant of

the deviatoric stress tensor ($J_2 = \frac{1}{2} \mathbf{s} : \mathbf{s}$). Here,

$$\omega = \frac{\tan \phi}{\sqrt{9 + 12 \tan^2 \phi}} \quad \text{and} \quad \psi = \frac{3c}{\sqrt{9 + 12 \tan^2 \phi}} \quad \text{are}$$

coefficients related to c and ϕ based on the Mohr-Coulomb failure criterion, and tensile stress is defined as positive. The stress tensor is denoted as $\boldsymbol{\sigma}$, and the deviatoric stress tensor is denoted as \mathbf{s} , leading to the following Eq. (1).

$$f(\boldsymbol{\sigma}) = \omega I_1 + \sqrt{J_2} - \psi = 0 \quad (1)$$

The stress $\boldsymbol{\sigma}$ in an object undergoing plastic deformation can be decomposed into the determined stress $\boldsymbol{\sigma}^{(1)}$, obtained from the plastic strain rate, and the undetermined stress $\boldsymbol{\sigma}^{(2)}$, which cannot be determined from the plastic strain rate. The determined stress $\boldsymbol{\sigma}^{(1)}$ is expressed as follows based on the associated flow rule.

$$\boldsymbol{\sigma}^{(1)} = \frac{\psi}{\sqrt{3\omega^2 + 0.5}} \frac{\dot{\boldsymbol{\epsilon}}^p}{\dot{\epsilon}} \quad (2)$$

where, $\dot{\boldsymbol{\epsilon}}^p$ represents the plastic strain rate, and $\dot{\epsilon} = \sqrt{\dot{\boldsymbol{\epsilon}}^p : \dot{\boldsymbol{\epsilon}}^p}$ represents the equivalent plastic strain rate. The undetermined stress $\boldsymbol{\sigma}^{(2)}$ consists of stress components along the linear portion of the yield function Eq. (1) and cannot be directly determined from the constitutive equation. However, by utilizing the fact that stress lies on the yield function, the components of undetermined stress can be expressed in Eq. (3). Applying the associated flow rule to the yield function Eq. (1) yields the condition for plastic strain rate (volumetric change characteristics).

$$h(\dot{\boldsymbol{\epsilon}}^p) = \dot{\epsilon}_v^p - \frac{3\omega}{\sqrt{3\omega^2 + 0.5}} \dot{\epsilon} = \dot{\epsilon}_v^p - \lambda \dot{\epsilon} = 0 \quad (3)$$

where, $\dot{\epsilon}_v^p$ is the plastic volumetric strain rate. Using the fact that Eq. (3) is a condition for plastic strain rate orthogonal to the yield function Eq. (1), $\boldsymbol{\sigma}^{(2)}$ can be expressed as follows using an undetermined coefficient α .

$$\boldsymbol{\sigma}^{(2)} = \alpha \frac{\partial h}{\partial \dot{\boldsymbol{\epsilon}}^p} = \alpha \left[\mathbf{I} - \frac{\Psi}{\sqrt{3\omega^2 + 0.5}} \frac{\dot{\boldsymbol{\epsilon}}^p}{\dot{\epsilon}} \right] \quad (4)$$

where, \mathbf{I} shows the unit tensor. Here, utilizing Eq. (2) and (4), we derive the elastic-plastic constitutive equation for the specified yield function, as expressed:

$$\boldsymbol{\sigma} = \boldsymbol{\sigma}^{(1)} + \boldsymbol{\sigma}^{(2)} = \frac{\Psi - 3\omega\alpha}{\sqrt{3\omega^2 + 0.5}} \frac{\dot{\boldsymbol{\epsilon}}^p}{\dot{\epsilon}} + \alpha \mathbf{I} \quad (5)$$

This constitutive equation includes the undetermined coefficient α . However, by conducting an analysis of boundary value problems along with the constraint conditions from Eq. (3), α can be determined. The elastic-plastic constitutive equation is suitable for deformable objects and not applicable to rigid bodies. However, for instability analysis, it becomes essential to examine rigid bodies. Therefore, the elastic-plastic constitutive equation is extended in Eq. (6); by performing an operation that replaces the equivalent plastic strain rate $\dot{\epsilon}$ with a threshold value $\dot{\epsilon}_0$ when $\dot{\epsilon}$ falls below this threshold value, Eq. (6) is obtained.

$$\begin{aligned} \boldsymbol{\sigma} &= \boldsymbol{\sigma}^{(1)} + \boldsymbol{\sigma}^{(2)} \\ &= \frac{\Psi - 3\omega\alpha}{\sqrt{3\omega^2 + 0.5}} \frac{\dot{\boldsymbol{\epsilon}}^p}{\dot{\epsilon}} + \alpha \mathbf{I} = \frac{\Psi - 3\omega\alpha}{\sqrt{3\omega^2 + 0.5}} \frac{\dot{\epsilon}}{\dot{\epsilon}_0} \frac{\dot{\boldsymbol{\epsilon}}^p}{\dot{\epsilon}} + \alpha \mathbf{I} \end{aligned} \quad (6)$$

This operation is effective in preventing division by zero in the rigid body region when the equivalent strain rate becomes small, as indicated in Eq. (5). Furthermore, the replacement by $\dot{\epsilon}_0$ has the effect of discounting the strength of the ground by $(\dot{\epsilon}/\dot{\epsilon}_0 < 1)$, thereby creating an equivalent reduction in shear strength. Therefore, Eq. (6) can be expected to have the same effect as creating a constitutive equation that appears to reduce shear strength, similar to Eq. (5), allowing for slight plastic deformation even in the rigid body portion. This enables the establishment of a similar structural relationship with respect to stress within the yield function, as in Eq. (6), and the ability to solve the equilibrium equation stably. The threshold value $\dot{\epsilon}_0$ is determined through numerical

experiments where $\dot{\epsilon}_0$ is varied beforehand, and a value that does not significantly affect the analytical solution is selected.

Hoshina et al. [19] developed a constitutive equation that integrated the strain rate constraint directly using the penalty method, a methodology also employed by [3, 4, 10, 13, 14, 15, 16]. The expression for the stress-strain rate relationship associated with the Drucker-Prager yield function is presented as follows:

$$\boldsymbol{\sigma} = \frac{\Psi}{\sqrt{3\omega^2 + 1/2}} \frac{\dot{\boldsymbol{\epsilon}}^p}{\dot{\epsilon}} + \kappa (\dot{\epsilon}_v^p - \lambda \dot{\epsilon}) \left(\mathbf{I} - \frac{3\omega}{\sqrt{3\omega^2 + 0.5}} \frac{\dot{\boldsymbol{\epsilon}}^p}{\dot{\epsilon}} \right) \quad (7)$$

By introducing a penalty constant denoted as " κ ," the integration of the Finite Element Method (FEM) with this constitutive equation enables an equivalent analysis of the upper bound theorem for plasticity, which is termed the RPFEM method within this research. A significant characteristic of this constitutive equation is its explicit definition of the stress-strain rate relationship. The rigid plastic constitutive equation is effective for its simplicity and efficiency in evaluating the soil's ultimate limit state. This offers a notable advantage by eliminating the necessity for uncertain elastic modulus values associated with the ground.

2.2. Application of rigid plastic constitutive equation to interface elements

This study aims to elucidate the relationship between stress and displacement velocity at the interface between the base of a footing and the ground surface during linear interactions involving various objects. It achieves this by employing a rigid-plasticity constitutive equation. An essential aspect of this research is the consideration of the discontinuity in the displacement velocity field at the contact surface. Additionally, it incorporates a stress vector ' \mathbf{t} ' governed by a Mohr-Coulomb-type yield function.

$$f(\mathbf{t}) = |t_s| - c_s + t_n \tan \phi_s = 0 \quad (8)$$

where, t_s and t_n represent the stress vector components acting along the shear and normal directions of the discontinuity line, while ϕ_s and c_s correspond to the frictional and cohesive strengths of the interface elements.

In this study, interface elements with zero thickness (a node-to-node element) are used into the contact plane between two bodies, as shown in Figure 1. The relative displacement velocity vector, denoted as $\Delta \dot{\mathbf{u}}$, is defined as the difference between the displacement velocity vectors at the (+) surface, $\dot{\mathbf{u}}^+$, and at the (-) surface, $\dot{\mathbf{u}}^-$.

The motion conditions associated with shear on the discontinuity line (volume change characteristics) are expressed by the following equation.

$$\begin{aligned} h(\Delta \mathbf{u}) &= |\Delta \dot{u}_s| \tan \phi_s - \Delta \dot{u}_n \\ &= \left(\Delta \dot{u}_s \cdot \frac{\tan \phi_s}{|\Delta \dot{u}_s|} - 1 \right) \begin{pmatrix} \Delta \dot{u}_s \\ \Delta \dot{u}_n \end{pmatrix} = \mathbf{a} \cdot \Delta \dot{\mathbf{u}} = 0 \end{aligned} \quad (9)$$

where, $\Delta \dot{u}_s, \Delta \dot{u}_n$ represent the relative displacement

velocity in the shear and normal directions, respectively. Similar to the soil material, when dividing the constitutive relationship into the determined stress $\mathbf{t}^{(1)}$ defined by the yield function equation and the undetermined stress $\mathbf{t}^{(2)}$, the following rigid-plastic constitutive equation is obtained.

$$\mathbf{t}^{(1)} = \gamma_s \frac{\partial f}{\partial \mathbf{t}} = \gamma_s \begin{pmatrix} \cos \phi_s \frac{\Delta \dot{\mathbf{u}}}{\|\Delta \dot{\mathbf{u}}\|} \\ \sin \phi_s \end{pmatrix} = \frac{c_s}{\cos \phi_s (1 + \tan^2 \phi_s)} \frac{\Delta \dot{\mathbf{u}}}{\|\Delta \dot{\mathbf{u}}\|} \quad (10)$$

$$\mathbf{t}^{(2)} = \omega_s \frac{\partial h}{\partial \Delta \dot{\mathbf{u}}} = \omega_s \begin{pmatrix} \tan \phi_s \frac{\Delta \dot{\mathbf{u}}}{\|\Delta \dot{\mathbf{u}}\|} \\ -1 \end{pmatrix} = \xi (\mathbf{a} \cdot \Delta \dot{\mathbf{u}}) \mathbf{a} \quad (11)$$

$$\mathbf{t} = \mathbf{t}^{(1)} + \mathbf{t}^{(2)} = \frac{c_s}{\cos \phi_s (1 + \tan^2 \phi_s)} \frac{\Delta \dot{\mathbf{u}}}{\|\Delta \dot{\mathbf{u}}\|} + \xi (\mathbf{a} \cdot \Delta \dot{\mathbf{u}}) \mathbf{a} \quad (12)$$

where, ξ is the penalty constant, and the constraint condition Eq. (11) is explicitly introduced into the constitutive equation.

Furthermore, $\|\Delta \dot{\mathbf{u}}\|$ represents the norm of the relative displacement velocity, and in the case of small relative displacement velocities, the operation of replacing $\|\Delta \dot{\mathbf{u}}\|$ with a threshold value $\|\Delta \dot{\mathbf{u}}\|_0$ threshold is used to describe the behavior of two objects behaving as one.

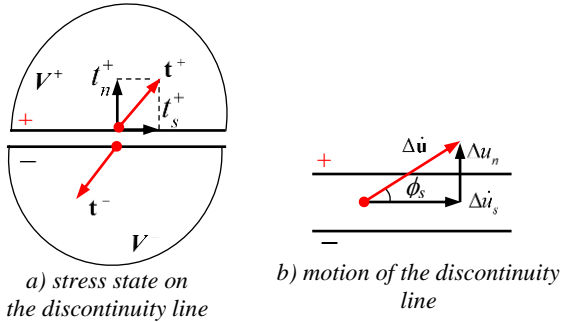


Figure 1. Vector of stress and velocity of relative displacement

3. Ultimate bearing capacity of rigid strip footing

3.1. Influence of footing roughness

As stated in the introduction, this main objective is to use a two-dimensional model for analyzing the behavior of the slope beneath a strip footing. A strip footing of width B is placed on a sandy soil slope with slope angle β and slope height H at an edge distance L from the crest of the slope, as shown in Figure 2. The investigation focuses on assessing the effect of slope geometry, including various slope angles (β ranging from 5° to 25°), edge distances (L from $0.0B$ to $5.0B$), and slope heights (H from $0.5B$ to $4.0B$). Figure 2 illustrates a typical finite element mesh and boundary conditions for simulating the footing-slope system, employing an interface element at the contact plane between the footing base and the soil surface. To ensure that the boundaries do not affect the failure mode or maximum bearing capacity of the rigid strip footing, the dimensions of the model were sufficiently large. A central point load was applied to a strip footing with a

width of $B=5.0$ m. The strip footing was simulated as a solid element with high strength to replicate a rigid footing. Both the strip footing and the sand slope are modeled as rigid perfectly plastic materials with specific properties: $\gamma_f = \gamma_{\text{soil}} = 18$ kN/m³, $c_f = 50.000$ kPa, and $\phi_f = 0$ deg. The internal friction angle of the sand slope varied from $\phi_{\text{soil}} = 30$ deg to 40 deg, and a small cohesion value ($c_{\text{soil}} = 0.5$ kPa) is applied to aid in the computational process. Two different friction conditions for the footing roughness were considered, and the interface element properties can be found in Table 1. Choosing the fine mesh size is crucial for improving simulation accuracy during model building. An iterative process is employed to determine the initial and final mesh sizes, with approximately 4000 initial elements and 6000 final elements chosen for reliable results. A fine mesh density near the footing base is maintained. The analysis revealed that the bearing capacity remained within a 0.5% difference when increasing the mesh to around 6000-7000 elements, affirming the effectiveness of boundary conditions. The study investigated four distinct failure modes: face failure, toe failure, base failure, and Prandtl-type failure, as illustrated in Figure 2.

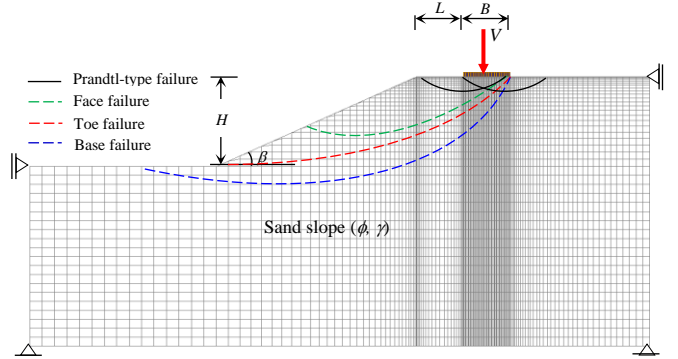


Figure 2. Boundary conditions for a strip footing subjected to a centrally applied vertical load on a sandy slope

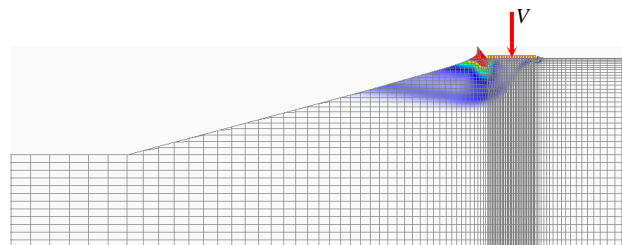
Table 1. Parameters for footing roughness

Parameter	Rough footing	Smooth footing
Internal friction angle ϕ_s ($^\circ$)	30, 35, 40	0
Cohesive strength c_s (kPa)	0.5	0.5

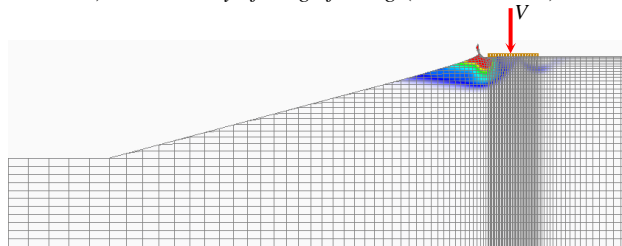
The maximum bearing capacity of the rigid strip footing was generally determined to be approximately $V=1975$ kN/m for rough footing, and approximately $V=1117$ kN/m for smooth footing. This represents about 57% of the value observed under rough footing, as illustrated in Figure 3. These results are consistent with the findings reported by Pham et al. [3] for horizontal sandy soil, where a 52% difference was observed between the two frictional conditions of the footing roughness.

Figure 3 shows for the norm strain rate distribution of the strip footing under a central vertical load. The norm strain rate, represented by contour lines, falls within a certain range ($0 - \dot{\epsilon}_{\text{max}}$). The distribution of the strain rate presents the failure mode of the strip footing, which is influenced by the footing roughness. Notably, the failure areas differ significantly due to the different footing roughness. Additionally, the rigid block formed beneath the footing base appears distinct between the rough and smooth footings.

The obtained failure mode closely resembles the slip line pattern observed in the rough footing as described in Pham et al. [10]. The failure mode involves one-sided failure into the slope in case of the rough footing (as shown in Figure 3a). Conversely, the failure mode is presented by two rigid triangular wedges in case of the smooth footing (as shown in Figure 3b). These wedges tend to move towards the two edges of the footing because the interface element of the smooth footing base permits horizontal movement. These numerical results from RPFEM underscore the significant effect of the footing roughness on both the ultimate bearing capacity and the failure mode of the footing-slope system.



a) In case study of rough footing ($V=1975$ kN/m)



b) In case study of smooth footing ($V=1117$ kN/m)

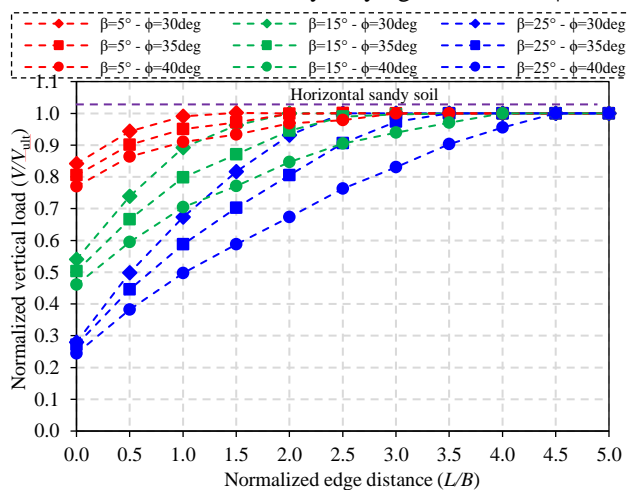
Figure 3. Deformation diagram of rigid strip footing on sandy slope of $\phi=30$ deg in case of $\beta=15^\circ$, $L=0.0B$, and $H=2.0B$

3.2. Effect of slope geometry on ultimate bearing capacity

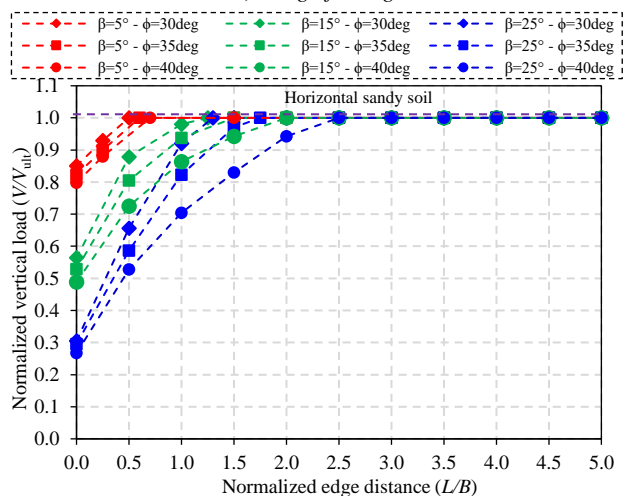
3.2.1. Effect of slope angle and edge distance

To assess the influence of slope angle β and edge distance L , a set of analyses was conducted across different values of ϕ (30 deg, 35 deg, and 40 deg). Figure 4 depicts the vertical load ratio (V/V_{ult}) in relation to the edge distance ratio (L/B) under both rough and smooth footings. In which, V_{ult} represents the ultimate bearing capacity of a strip footing on horizontal sandy soil. These results reveal that an increase in the slope angle (β) leads to a reduction in the ultimate bearing capacity. Importantly, it's noteworthy that the ultimate bearing capacity of the footing-slope system consistently falls within the range of values applicable to horizontal sandy soil, irrespective of the footing's roughness. These plots clearly illustrate that augmenting the edge distance (L) enhances the ultimate bearing capacity. When the edge distance (L) reaches a critical value, denoted as L_{cr} , the bearing capacity stabilizes at a constant level, similar to that of horizontal sandy soil. The value of the critical distance L_{cr} seems to be influenced by the internal friction angle ϕ . Furthermore, it's observed that the critical distance L_{cr} is greater for the rough footing compared to the smooth footing. Consequently, increasing the edge distance does not substantially impact the ultimate bearing capacity, regardless of the footing roughness. In Figure 4, for a standard case with $\phi=30$ deg, it is determined that the critical distance L_{cr} is approximately

$2.0B$ for the rough footing, while it is about $1.25B$ for the smooth footing. This outcome aligns well with the findings of Meyerhof [6]. These results suggest that the RPFEM method can reasonably predict both the bearing capacity and the critical distance L_{cr} by varying the value of ϕ .



a) Rough footing

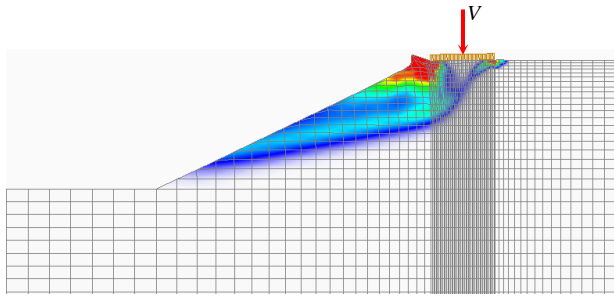


b) Smooth footing

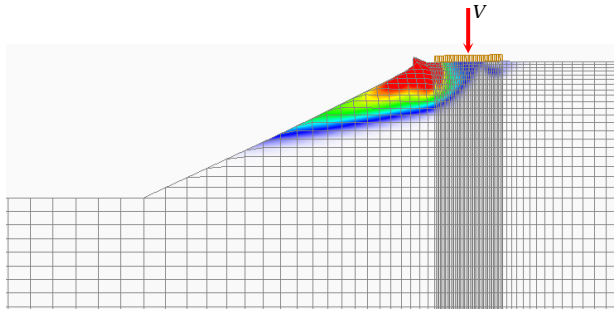
Figure 4. Effect of slope angle β , and edge distance L on normalized vertical load (V/V_{ult}) in case of $H=2.0B$

Furthermore, Figure 5 indicates the failure modes of the strip footing on a sandy slope of $\phi=30$ deg being depicted for rough and smooth footings when dealing with a high slope angle of $\beta=25^\circ$. These failure mechanisms exhibit distinctive characteristics. In one mechanism, toe failure is observed for the rough condition (as seen in Figure 5a), while the other mechanism illustrates a face failure for the smooth condition (as depicted in Figure 5b). In comparison to $\beta=15^\circ$, shown in Figure 3, the failure zone has extended further towards the crest side of the slope. This extension results from the unfavorable impact of soil weight, acting as an external force that initiates instability in the footing-slope system. It becomes clear that as the slope angle β increases, the failure mechanism shifts from the face failure mechanism to the toe failure mechanism. In the case of a rough surface condition, the strip footing achieves its maximum bearing capacity at around $V=1023$ kN/m, whereas under smooth conditions, this capacity is approximately $V=605$ kN/m. This

underscores the substantial influence of β on the ultimate bearing capacity. As a result, with a continued increase in the slope angle β , the footing-slope system eventually experiences a gravity-induced overall failure mode.

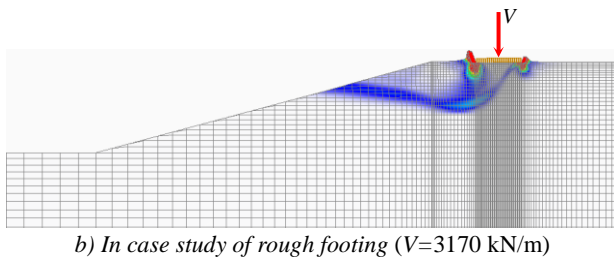


a) In case study of rough footing ($V=1023$ kN/m)

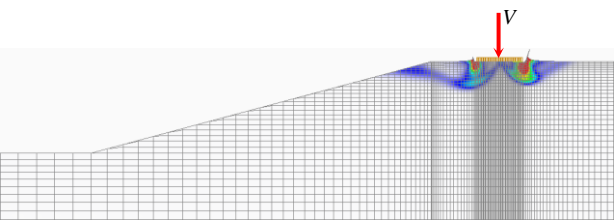


b) In case study of smooth footing ($V=605$ kN/m)

Figure 5. Deformation diagrams of strip footing on sand slope of $\phi=30$ deg for high slope angle $\beta=25^\circ$, $L=0.0B$, and $H=2.0B$



a) In case study of rough footing ($V=3170$ kN/m)



b) In case study of smooth footing ($V=1943$ kN/m)

Figure 6. Deformation diagram of strip footing on sand slope of $\phi=30$ deg for large edge distance $L=1.0B$, $\beta=15^\circ$, and $D=2.0B$

Figure 6 provides additional clarity on the failure patterns observed in the footing-slope system, particularly when considering a substantial edge distance ($L=1.0B$) for both rough and smooth footings. These failure patterns commonly manifest when a rigid footing is situated at a distance from the slope's crest, akin to conditions observed in horizontal sandy soil, as previously discussed in the research conducted by Loukidis et al. [20] and Pham et al. [3, 4, 21, 22]. It becomes apparent that augmentation of the edge distance (L) results in a transition of the failure mode from face failure to a Prandtl-type failure. In the RPFEM computation, the ultimate bearing capacity of the strip

footing closely resembles that observed on horizontal sandy soil. Specifically, it reaches approximately $V=3170$ kN/m for the rough footing and $V=1943$ kN/m for the smooth footing. The substantial edge distance ensures that the slip surface develops within the horizontal sandy soil, diminishing the slope's effect. These findings are in concordance with research outcomes from [6], [10], collectively contributing to a more comprehensive understanding of how slope geometry impacts the bearing capacity of the rigid strip footing.

3.2.2. Effect of slope height

To investigate the influence of slope height, a series of analyses were performed, varying the slope height H from $0.5B$ to $4.0B$. Consistent with previous findings by [6], [10], it was observed that the ultimate bearing capacity of the footing-slope system remains stable when the slope height exceeds the depth of the slip surface. However, it's worth noting that a different pattern emerges when dealing with a small slope height of $H=0.5B$ combined with a high slope angle of $\beta=25^\circ$, as shown in Figure 7. This phenomenon can be attributed to variations in the strip footing's failure zone, where the failure mechanism can encompass either toe or base failure modes across all analyzed scenarios.

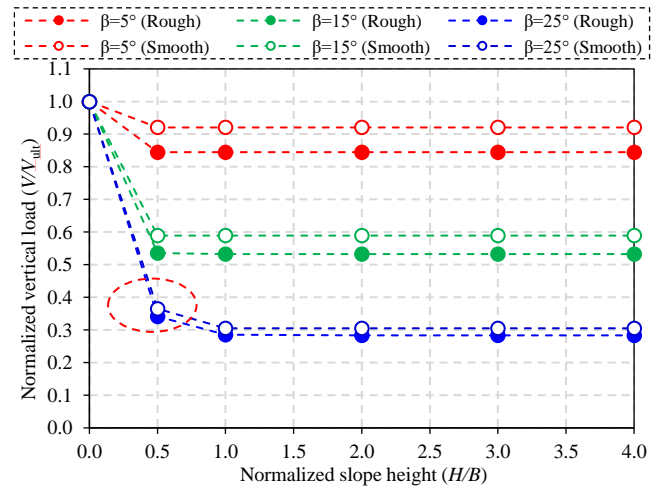


Figure 7. Effect of slope height H on normalized vertical load (V/V_{ult}) in a case study of $L=0.0B$ and sand slope of $\phi=30$ deg

Figure 8 illustrates the failure mode of a rigid strip footing positioned on the crest slope. This analysis considers both rough and smooth footings with a high slope angle ($\beta=25^\circ$) and a small slope height ($H=0.5B$). In this particular scenario, base failures dominate, characterized by the failure slip area extending from the edge of the footing to beneath the slope's toe. This type of failure mode has the potential to mobilize greater shear resistance compared to face or toe failure modes, and the passive resistance increases as the slope's influence diminishes. The computed ultimate bearing capacity of the strip footing in this case is approximately $V=1226$ kN/m for the rough footing and about $V=756$ kN/m for the smooth footing, representing 59% of that observed in the rough footing. When comparing Figures 5 and 8 for $H=2.0B$ and $H=0.5B$, it becomes evident that the slope's effect on the bearing capacity decreases significantly. This increase in the collapse load is attributed to the rise in passive resistance

beneath the footing base. The results obtained from RPFEM provide valuable insights into how slope height impacts the ultimate bearing capacity and failure modes of the rigid strip footing.

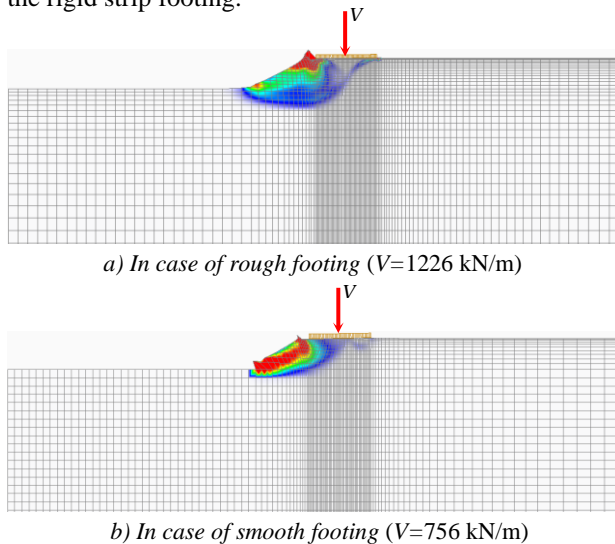


Figure 8. Deformation diagrams of strip footing in case of small slope height $H=0.5B$, and high slope angle of $\beta=25^\circ$ ($\phi=30^\circ$)

4. Conclusions

Key conclusions drawn from the study are as follows:

(1) A new constitutive equation for the interface element successfully introduced the contact plane between the footing base and the ground surface. It was found that the solution was positively effective for analyzing the interaction between the footing base and the soil surface. The model demonstrated its precision in emulating two distinct conditions: rough and smooth. The roughness of the footing surface proved to be a pivotal factor in influencing various failure modes, notably the rigid triangular wedge mode, and the two rigid triangular wedges mode.

(2) The study extensively delved into the impact of slope geometry on the ultimate bearing capacity, considering both rough and smooth conditions. Across a range of case studies, it became evident that the ultimate bearing capacity of the footing-slope system exhibited a decline as the slope angle increased, regardless of the footing roughness. However, an expansion in the edge distance led to an increase in the ultimate bearing capacity, up to a critical distance L_{cr} . The specific value of L_{cr} was contingent upon factors such as the slope angle (β), internal friction angle (ϕ), and footing roughness. Additionally, minor variations were observed when altering the slope height (H). The research identified four distinct failure modes, each shaped by the interplay of slope geometry and footing roughness.

Acknowledgment: PHAM Ngoc Quang received a Postdoctoral Scholarship with code VINIF.2022.STS.53 from the Vingroup Innovation Foundation (VINIF).

REFERENCES

[1] C. Tang, P. Kok-Kwang, and T. Kim-Chuan, "Effect of footing width on N_γ and failure envelope of eccentrically and obliquely loaded strip footings on sand", *Canadian Geotechnical Journal*, vol.

52, no. 6, pp. 694-707, 2015.

[2] G. Zheng, Z. Jiapeng, Z. Haizuo, and Z. Tianqi, "Ultimate bearing capacity of strip footings on sand overlying clay under inclined loading", *Computers and Geotechnics* 106, 266-273, 2019.

[3] N.Q. Pham, S. Ohtsuka, K. Isobe, Y. Fukumoto, and T. Hoshina, "Ultimate bearing capacity of rigid footing under eccentric vertical load", *Soils and Foundations*, vol. 59, no. 6, 1980-1991, 2019.

[4] N.Q. Pham, S. Ohtsuka, K. Isobe, and Y. Fukumoto, "Limit load space of rigid footing under eccentrically inclined load", *Soils and Foundations*, vol. 60, no. 4, 811-824, 2020.

[5] G. Jim, M. Andrews, and D. H. Shields, "Stress characteristics for shallow footings in cohesionless slopes", *Canadian Geotechnical Journal*, vol. 25, no. 2, 238-249, 1988.

[6] G.G. Meyerhof, "The ultimate bearing capacity of foundations on slopes", In *Proc., 4th Int. Conf. on Soil Mechanics and Foundation Engineering*, vol. 1, 1957, pp. 384-386

[7] X. Yao, M. Zhao, R. Zhang, H. Zhao, and G. Wu, "Undrained bearing capacity of strip footings placed adjacent to two-layered slopes", *International Journal of Geomechanics*, vol. 19, no. 8, 06019014, 2019.

[8] Z. Haizuo, G. Zheng, X. Yang, T. Li, and P. Yang, "Ultimate seismic bearing capacities and failure mechanisms for strip footings placed adjacent to slopes", *Canadian Geotechnical Journal*, vol. 56, no. 11 1729-1735, 2019.

[9] W. Gaoqiao, R. Zhang, M. Zhao, and S. Zhou, "Undrained stability analysis of eccentrically loaded strip footing lying on layered slope by finite element limit analysis", *Computers and Geotechnics*, vol. 123, p. 103600, 2020.

[10] N.Q. Pham, S. Ohtsuka, K. Isobe, N.V. Pham, and P.H. Hoang, "Limit load space of rigid strip footing on sand slope subjected to combined eccentric and inclined loading", *Computers and Geotechnics*, vol. 162, p. 105652, 2023.

[11] C. Li, A. Zhou, and P. Jiang, "Eccentric bearing capacity of embedded strip footings placed on slopes", *Computers and Geotechnics*, vol. 119, p. 103352, 2020.

[12] S. Yang, B. Leshchinsky, K. Cui, F. Zhang, and Y. Gao, "Influence of failure mechanism on seismic bearing capacity factors for shallow foundations near slopes", *Géotechnique*, vol. 71, no. 7, pp. 594-607, 2021.

[13] N.Q. Pham, and S. Ohtsuka, "Ultimate bearing capacity of rigid footing on two-layered soils of sand-clay", *International Journal of Geomechanics* 21, no. 7, 04021115, 2021.

[14] N.Q. Pham, S. Ohtsuka, K. Isobe, and Y. Fukumoto, "Limit load space of rigid strip footing on cohesive-frictional soil subjected to eccentrically inclined loads", *Computers and Geotechnics* 151, 104956, 2022.

[15] N.Q. Pham, S. Ohtsuka, K. Isobe, and PH. Hoang, "Ultimate bearing capacity of rigid strip footings on c- ϕ soil subjected to combined eccentric and inclined loading", In *IOP Conference Series: Materials Science and Engineering*, vol. 1289, no. 1, IOP Publishing, 2023, p. 012088.

[16] N.Q. Pham, S. Ohtsuka, K. Isobe, and Y. Fukumoto, "Group effect on ultimate lateral resistance of piles against uniform ground movement", *Soils and Foundations*, vol. 59, no. 1, pp. 27-40, 2019.

[17] T. Tamura, S. Kobayashi, and T. Sumi, "Rigid-plastic finite element method for frictional materials", *Soils and Foundations*, vol. 27, no. 3, pp. 1-12, 1987.

[18] A. Asaoka and S. Ohtsuka, "Bearing capacity analysis of a normally consolidated clay foundation", *Soils and foundations*, vol. 27, no. 3, 58-70, 1987.

[19] T. Hoshina, "Rigid plastic stability analysis for slope including thin weak layer", *Japanese Geotechnical Journal*, vol. 6, no. 2, 191, 2011.

[20] D. Loukidis, T. Chakraborty, and R. Salgado, "Bearing capacity of strip footings on purely frictional soil under eccentric and inclined loads", *Canadian Geotechnical Journal*, vol. 45, no. 6, pp. 768-787, 2008.

[21] N.Q. Pham and S. Ohtsuka, "Numerical Investigation on Bearing Capacity of Rigid Footing on Sandy Soils Under Eccentrically Inclined Load", In *Proceedings of the 2nd Vietnam Symposium on Advances in Offshore Engineering: Sustainable Energy and Marine Planning*, Vol. 208, Springer Singapore, 2022, pp. 333-341. DOI:10.1007/978-981-16-7735-9 37

[22] N.Q. Pham, S. Ohtsuka, K. Isobe, and Y. Fukumoto, "Consideration on Limit Load Space of Footing on Various Soils Under Eccentric Vertical Load", In *Challenges and Innovations in Geomechanics: Proceedings of the 16th International Conference of IACMAG*, Volume 126, Springer International Publishing, 2021, pp. 75-84.